Schweizerische Eidgenossenschaft
Confédération suisse
Confederazione Svizzera
Confederaziun svizra

Federal Department of the Environment,
Transport, Energy and Communications DETEC

Swiss Federal Office of Energy
Energy Research and Cleantech

Final report from 12 September 2025

REVERSO

Receiver for Concentrated Solar Power

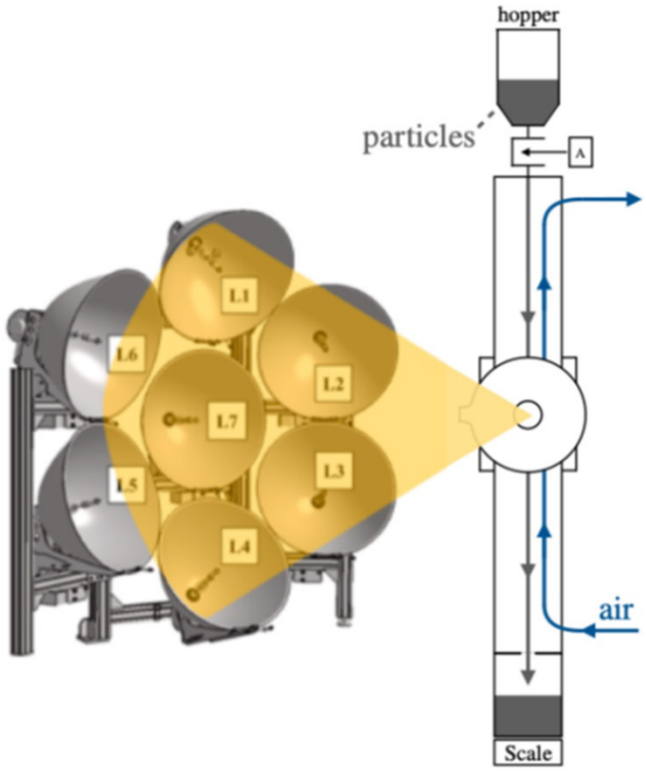

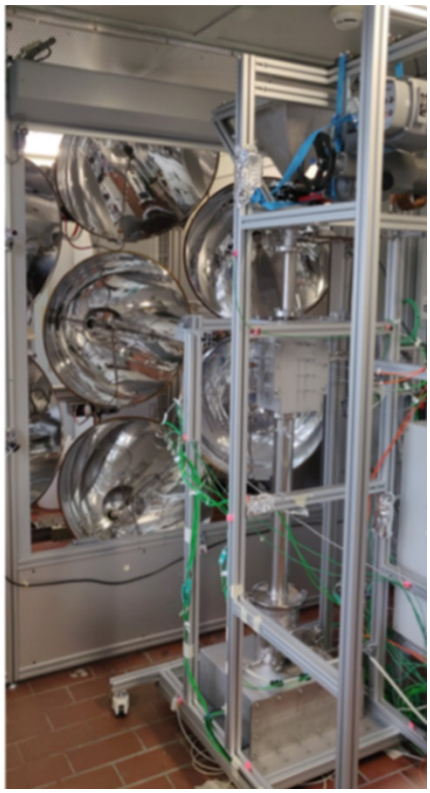

Publisher:
Swiss Federal Office of Energy SFOE
Energy Research and Cleantech
CH-3003 Berne
www.energy-research.ch

Subsidy recipients:
ETH Zurich
Institute of Fluid Dynamics (IFD)
Professorship for Experimental Fluid Dynamics (EFD)
Sonneggstrasse 3, CH-8092 Zurich
https://exp.ethz.ch

ETH Zurich
Institute of Energy Technology
Professorship of Renewable Energy Carriers (PREC)
Sonneggstrasse 3, CH-8092 Zurich
https://prec.ethz.ch

Authors:
Anton Hartner, ETH Zurich, EFD, ahartner@ethz.ch
Prof. Dr. Filippo Coletti, ETH Zurich, EFD, fcoletti@ethz.ch
Prof. Dr. Aldo Steinfeld, ETH Zurich, PREC, aldo.steinfeld@ethz.ch

SFOE project coordinators:
Dr. Stefan Oberholzer, stefan.oberholzer@bfe.admin.ch

SFOE contract number: SI/502302-01

Summary

Concentrated solar power (CSP) is a renewable energy technology that converts the radiative energy provided by the sun into high-temperature heat by raising the temperature of a heat transfer medium (HTM) to 700◦C and above. Therefore, it is one of the few sustainable alternatives that has the potential to replace fossil burners that are currently used in processes that demand high-temperature heat. One of the key components that significantly influences the overall efficiency of a process operated with CSP is the solar receiver. It is here that the radiative energy from the sun is transferred to the heat transfer medium, which can be gaseous, liquid or solid.

The project REVERSO was launched to design and investigate an indirectly irradiated particle solar receiver, in which ceramic particles are used as the HTM. The ceramic particles are supplied to the receiver and their fall speed decreased by setting a counter-current air flow. Having a means to control the fall speed of the particles allows to influence the residence time of the particles inside the receiver, which has a direct influence on the particle outlet temperature. The particle residence time is a desirable control parameter when it comes to the conversion of chemical reactions or adapting to a changing energy supply to the receiver due to solar intermittency (e.g.: course of the sun, clouds). Already existing solar particle receivers either lack the ability to control the residence time of the particles in the receiver, or they are rather complex and consume considerable amounts of energy during operation.

Throughout the REVERSO project, the counter-current particle-air receiver was designed, manufactured on a laboratory scale and its fluid dynamics and thermal performance were investigated. It could be shown that such a receiver can be safely operated and that the presence of the air flow increases the average particle outlet temperature, the thermal efficiency as well as the local wall-to-particles heat transfer coefficient compared to scenarios without air. So far, temperatures of up to 795 °C with a thermal efficiency of 31 % were achieved and it is believed that a scaled up version of the receiver is able to deliver outlet temperatures exceeding 1000 °C. Velocity field measurements of the particle phase at room temperature revealed that the falling velocity of the particles decreases as a function of the amount of air supplied to the system. However, in order to better understand how well the counter-current air flow can be used as a control parameter for the residence time of the particles in the receiver, further investigations at higher temperatures are required. A simulation of the novel receiver is currently being developed and will be compared with the experimental data. This simulation can be used to further refine the design for the next generation of the particle receiver. The REVERSO project was intended to show whether such a new type of particle receiver can be operated safely and proofed that the presence of the counter-current air flow increases its thermal performance.

If the work on the particle receiver is to be continue, it is crucial to achieve particle outlet temperatures of 1000 °C and to show that this is possible while realizing thermal efficiencies of over 50%. Increasing the size of the receiver is one way to reduce the disadvantage˙ of the currently very high surface-to-volume ratio, but it may also be worth adapting the design so that direct irradiation of the particles is possible and eliminate the heat transfer resistance from the tube to the particles.

Zusammenfassung

Konzentrierte Solarenergie (CSP, Concentrated Solar Power) ist eine erneuerbare Energietechnologie, bei der die Strahlungsenergie der Sonne genutzt wird, um ein Wärmeträgermedium auf Temperaturen von über 700 °C zu erhitzen. CSP ist eine der wenigen nachhaltigen Alternativen, die das Potenzial haben, fossile Prozesse zu ersetzen, wie sie derzeit in Industrien mit hohem Wärmebedarf zum Einsatz kommen. Der Solarabsorber ist eine der Schlüsselkomponenten, die die Gesamteffizienz eines CSP-basierten Prozesses massgeblich beeinflussen. Ein Wärmeträgermedium, das gasförmig, flüssig oder fest sein kann, wird durch den mit Sonnenlicht bestrahlten Absorber geleitet, wobei es sich erwärmt.

Im Rahmen des Projekts REVERSO wurde ein indirekt bestrahlter Partikel-Solarabsorber entwickelt und untersucht, bei dem keramische Partikel als Wärmeträgermedium eingesetzt werden. Die keramischen Partikel werden dem Absorber zugeführt, wobei ihre Fallgeschwindigkeit durch einen gegenläufigen Luftstrom gezielt verringert wird. Die Möglichkeit, die Fallgeschwindigkeit der Partikel zu variieren, erlaubt es, deren Verweilzeit im Absorber gezielt zu beeinflussen, was wiederum einen direkten Einfluss auf die Auslasstemperatur der Partikel hat. Die Verweilzeit der Partikel stellt einen wichtigen Regelparameter dar, insbesondere im Zusammenhang mit chemischen Reaktionen oder zur Anpassung an eine schwankende Energiezufuhr, etwa durch Wolken oder den Tageszyklus der Sonne. Bereits existierende Partikelabsorber verfügen entweder nicht über die Möglichkeit, die Verweilzeit der Partikel zu regeln, oder sie sind konstruktiv sehr komplex und verbrauchen im Betrieb nicht vernachlässigbare Energiemengen.

Im Verlauf des Projekts wurde der Absorber im Labormassstab konstruiert, gefertigt und hinsichtlich seiner Strömungs- sowie Wärmeübertragungseigenschaften untersucht. Es konnte gezeigt werden, dass der Absorber sicher betrieben werden kann und dass der Luftstrom die gemittelte Auslasstemperatur der Partikel, die thermische Effizienz sowie den lokalen Wärmeübergangskoeffizienten zwischen Wand und Partikeln erhöht. Bisher konnten Temperaturen von bis zu 795 °C mit einer thermischen Effizienz von 31 % erreicht werden. Es wird angenommen, dass eine hochskalierte Version des Absorbers Partikeltemperaturen von über 1000 °C liefern kann. Messungen des Geschwindigkeitsfeldes der Partikel bei Raumtemperatur zeigten, dass die Fallgeschwindigkeit der Partikel in Abhängigkeit von der zugeführten Luftmenge abnimmt. Um besser zu verstehen, inwieweit der Luftstrom als Regelparameter für die Verweilzeit der Partikel im Absorber genutzt werden kann, sind weitere Untersuchungen bei höheren Temperaturen erforderlich. Eine Simulation des neuartigen Absorbers wird derzeit entwickelt und zukünftig mit den experimentellen Daten verglichen. Diese Simulation kann dazu beitragen, das Design der nächsten Generation des Partikelabsorbers weiter zu optimieren. Das Projekt REVERSO konnte zeigen, dass das neue Absorber-Konzept sicher betrieben werden kann und hat den Nachweis erbracht, dass der Luftstrom die thermische Leistungsfähigkeit des Absorbers signifikant verbessert.

Für die Fortsetzung der Arbeiten am Partikelabsorber ist es entscheidend, Partikelauslasstemperaturen von 1000 °C zu erreichen und gleichzeitig thermische Wirkungsgrade von über 50 % nachzuweisen. Eine hochskalierte Version des Absorbers ist eine Möglichkeit, den Nachteil des derzeit sehr hohen Oberflächen-Volumen-Verhältnisses zu verringern. Es könnte jedoch auch sinnvoll sein, das Design so anzupassen, dass eine direkte Bestrahlung der Partikel möglich wird und der Wärmeübergangswiderstand zwischen Rohrwand und Partikeln entfällt.

Résumé

L'énergie solaire concentrée (CSP, Concentrated Solar Power) est une technologie d'énergie renouvelable qui utilise l'énergie rayonnante du soleil pour chauffer un fluide caloporteur à des températures supérieures à 700 °C. La CSP est l'une des rares alternatives durables susceptibles de remplacer les processus fossiles actuellement utilisés dans les industries à forte demande thermique. L'absorbeur solaire est l'un des composants clés qui influencent de manière significative l'efficacité globale d'un processus basé sur la CSP. Un fluide caloporteur, qui peut être gazeux, liquide ou solide, est acheminé à travers l'absorbeur exposé au rayonnement solaire, où il est chauffé.

Dans le cadre du projet REVERSO, un absorbeur solaire à particules à irradiation indirecte a été développé et étudié, dans lequel des particules céramiques sont utilisées comme fluide caloporteur. Les particules céramiques sont acheminées vers l'absorbeur, leur vitesse de chute étant réduite de manière ciblée par un flux d'air à contre-courant. La possibilité de varier la vitesse de chute des particules permet d'influencer de manière ciblée leur temps de séjour dans l'absorbeur, ce qui a à son tour une influence directe sur la température de sortie des particules. Le temps de séjour des particules est un paramètre de régulation important, notamment en relation avec les réactions chimiques ou pour s'adapter à un apport énergétique variable, par exemple en raison des nuages ou du cycle quotidien du soleil. Les absorbeurs de particules existants n'offrent pas la possibilité de réguler le temps de séjour des particules ou sont de conception très complexe et consomment des quantités d'énergie non négligeables pendant leur fonctionnement.

Au cours du projet, l'absorbeur a été conçu et fabriqué à l'échelle du laboratoire, puis testé en termes de propriétés d'écoulement et de transfert de chaleur. Il a été démontré que l'absorbeur peut fonctionner en toute sécurité et que le flux d'air augmente la température moyenne de sortie des particules, l'efficacité thermique et le coefficient de transfert thermique local entre la paroi et les particules. Jusqu'à présent, des températures allant jusqu'à 795 °C ont pu être atteintes avec une efficacité thermique de 31 %. On suppose qu'une version à grande échelle de l'absorbeur peut fournir des températures de particules supérieures à 1000 °C. Les mesures du champ de vitesse des particules à température ambiante ont montré que la vitesse de chute des particules diminue en fonction de la quantité d'air fournie. Afin de mieux comprendre dans quelle mesure le débit d'air peut être utilisé comme paramètre de régulation du temps de séjour des particules dans l'absorbeur, des études supplémentaires à des températures plus élevées sont nécessaires. Une simulation du nouvel absorbeur est actuellement en cours de développement et sera comparée à l'avenir aux données expérimentales. Cette simulation peut contribuer à optimiser davantage la conception de la prochaine génération d'absorbeurs de particules. Le projet REVERSO a montré que le nouveau concept d'absorbeur peut être exploité en toute sécurité et a prouvé que le flux d'air améliore considérablement les performances thermiques de l'absorbeur.

Pour poursuivre les travaux sur l'absorbeur de particules, il est essentiel d'atteindre des températures de sortie des particules de 1 000 °C tout en démontrant des rendements thermiques supérieurs à 50 %. Une version à grande échelle de l'absorbeur est un moyen de réduire l'inconvénient du rapport surface/volume actuellement très élevé. Cependant, il pourrait également être judicieux d'adapter la conception de manière à permettre un rayonnement direct des particules et à éliminer la résistance au transfert de chaleur entre la paroi du tube et les particules.

Main findings («Take-Home Messages»)

- A laboratory-scale particle receiver, in which submillimeter particles fall against an upward airflow, was designed, realized and tested for high-temperature operation, leveraging a high-flux solar simulator that mimics solar concentrating systems. The objective was to increase the amount of heat absorbed by the particles by extending their residence time in the radiated section.
- Imaging of the particle transport in a transparent replica of the receiver confirmed that the counter-current airflow induces a significant deceleration of the particle phase. At low particle mass flow rates, the flow promotes a homogenized particle concentration across the channel width, while clustering ensues at higher particle mass flow rates.
- In presence of the counter-current airflow, the particle outlet temperature, thermal efficiency, and wall-to-particle heat transfer coefficient were increased compared to the case without airflow. The limited range of parameters accessible in the laboratory, however, did not allow the identification of a clear trend with increasing airflow or the presence of an optimum.
- The receiver's performance appeared comparable with other particle-in-tube concepts, while offering operational simplicity. Although the current study did not reach the target outlet temperature of 1000°C, the high operating temperatures achieved in the cavity indicated the potential for applicability of the novel concept, which shall be tested in scaled-up installations.

Contents

List of abbreviations

CAD	Computer-aided design
CFDR	Counter-flow downer receiver
CSP	Concentrated solar power
EFD	Experimental fluid dynamics group at ETH Zurich
HFSS	High-Flux solar simulator
HSM	Heat storage medium
HTC	Heat transfer coefficient
HTM	Heat transfer medium
KPI	Key performance indicators
MFC	Mass flow controller
MCRT	Monte Carlo ray-tracing
LCOE	Levelized cost of energy
PIV	Particle image velocimetry
PSD	Particle size distribution
PREC	Professorship of renewable energy carriers at ETH Zurich
REVERSO	Receiver for concentrated solar power
RTD	Residence time distribution
SFOE	Swiss Federal Office of Energy
SiC	Silicon carbide
SPR	Solar particle receiver
StoA	State of the art
TCs	Thermocouples
TES	Thermal energy storage
TRL	Technology readiness level

List of Symbols

C	Concentration Ratio
$c_{p,i}$	specific heat capacity of component *i*
d_p	particle diameter
h_i	specific enthalpy of component *i*
$h(z)$	local heat transfer coefficient at height *z*
k_t	thermal conductivity of the tube material
$\dot{m}_i$	mass flow rate of component *i*
$\dot{Q}_{\mathrm{solar}}$	radiative power input supplied by the HFSS
$\mathrm{Re}_{\mathrm{bulk}}$	Reynolds bulk number (based on air velocity)
$T_{d,ext}(@\,z)$	external tube wall temperature at height *z*
$T_{d,int}(@\,z)$	internal tube wall temperature at height *z*
u_t	terminal velocity of a single sphere in stil air
$\dot{V}_i$	volumetric flow rate of component *i*
$\langle \overline{w}(z) \rangle_z$	temporally averaged vertical velocity component profiles, averaged over the z-component
η_{th}	thermal efficiency
ρ_i	density of component *i*
$\phi_{v,i}$	volume fraction of component *i*

1 Introduction

1.1 Background Information & Current Situation

In concentrated solar power (CSP) the non-polluting, clean radiant energy of the sun is collected by a set of mirrors, which redirect the incoming irradiation towards a device called solar receiver. Inside the solar receiver, the radiative energy is absorbed by a heat transfer medium (HTM) resulting in the conversion of radiative energy into thermal energy (see figure 1). The obtained thermal energy can be used for the generation of electricity, as high temperature process heat, or to drive highly endothermic chemical reactions like the production of synthetic fuels. Furthermore, it is possible to store the thermal energy in a thermal energy storage unit (TES) allowing to deliver heat round-the-clock.[1–3] The combination of CSP with TES enables more reliable and secure energy generation compared to other, more intermittent renewable energy technologies such as wind energy or photovoltaics.[4]

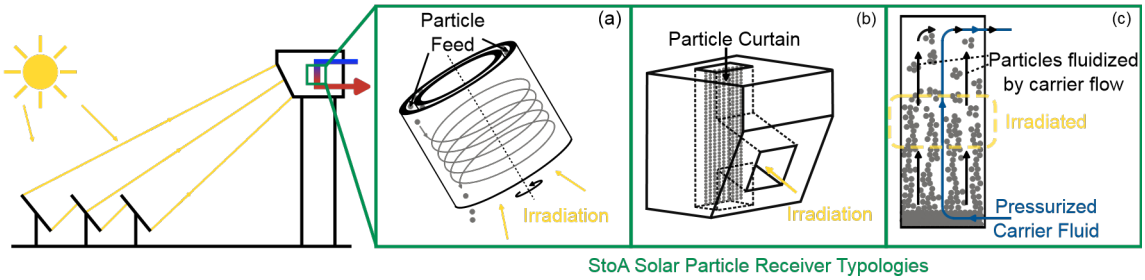

Figure 1: In a central receiver CSP plant configuration, the incoming irradiation is redirected by a field of mirrors, the heliostat field, towards the top of a tower. At the top of the tower a solar receiver is located in which the radiative energy of the sun is transformed into thermal energy by heating up a heat HTM. For solar receivers using particles as HTM three state of the art typologies exist: (a) the rotary kiln receiver, (b) the particle curtain receiver and (c) the fluidized bed receiver.[5]

In general, solar receivers are distinguished by the aggregate state of the HTM used and by whether the HTM is irradiated directly or indirectly. When targeting HTM outlet temperatures above 1000 °C, the physical state of the HTM is best gaseous or solid, since current state of the art (StoA) liquid HTM start to decompose at temperatures above 600 °C.[6,7] The direct irradiation of the HTM leads to a lower heat transfer resistance compared to indirectly irradiated receivers, where the compartment through which the HTM flows, e.g. a tube, is heated by the incident radiation and the heat is absorbed by the HTM from the inner wall of the compartment.[8] However, certain receiver configurations require a compartment to contain the HTM and cannot be manufactured from optically transparent materials such as quartz as it will break at these elevated temperatures, especially if cooling is not an option.

For CSP technology to become cost competitive in the future, solar receivers must deliver HTM outlet temperatures exceeding 700 °C while maintaining high thermal efficiencies. In addition, they should have low parasitic energy losses, be easy to operate, and be scalable for deployment in large CSP plants. Outlet temperatures above 700 °C are necessary to facilitate the use of the more efficient Brayton cycle and to enable the substitution of fossil-fueled processes in high-energy, high-temperature applications such as the production of cement and ammonia. Mehos et al.[9] identified that particle solar receivers have the potential to satisfy these goals. Another major advantage of working with a solar particle receiver (SPR) is that the particles also serve as a heat storage medium (HSM), which significantly increases the efficiency of the TES.

Currently, three StoA typologies of SPR are reported in literature.[5] The first typology, the particle curtain receiver, works with a particle film created by distributing particles through a thin slot on the top of the receiver. Then, driven by gravity, the particles fall through an irradiated section. The second typology,

called rotating kiln receiver, consists of a drum which rotates around its central axis. Particles are fed at the top of the drum and run down along the drum wall due to centrifugal force. The drum has an opening at the bottom through which the particles are irradiated directly. Finally, the fluidized-bed receiver consists of one or more tubes in which the particles are fluidized by means of a carrier fluid that transports them through an irradiated section. Depending on the tube material, they can be irradiated directly or indirectly (quartz vs. ceramic material). Table 1 contains a comparison between the different SPR concepts based on six important questions:

a. Is it possible to control the particle residence time (PRT) inside the irradiated area?
b. Is it possible to change the particle concentration?
c. How stable does the receiver operate? Are parasitic energy losses present?
d. Are the particles directly or indirectly irradiated?
e. Are particles lost to the environment?
f. Can the reaction environment be controlled?

The particle curtain receiver typology lacks the option to tune the residence time of the particles inside the irradiated area, such that an important control parameter for adjusting the particle outlet temperature is absent. This control parameter is of special interest to react to the intermittency of the sun and when targeting one step thermochemical processes, where the residence time of the reactants is directly linked to the conversion of the reaction.[10] Both the fluidized bed and the rotary kiln receiver allow the PRT to be tuned, but they are rather complex systems, difficult to operate and suffer from high parasitic energy losses. High parasitic energy losses mean that a non-negligible amount of energy is required to operate these receivers, which leads to a reduction in the overall efficiency of the process and should therefore be as low as possible. Another problem with open-aperture, directly irradiated receivers like the particle curtain receiver and the rotary kiln receiver, is that they are suffering from considerable particle loss due to interactions with wind.[9] Thermochemical processes often require a controlled reaction environment that differs from ambient air, which can only be maintained if the reaction occurs within a closed system. With this in mind, a novel indirectly irradiated SPR concept was formulated, the *counter-flow downer receiver* (CFDR). The CFDR offers a complementary approach that tackles shortcomings of existing SPRs (see table 1). In general, if CSP technology is to be employed across a range of processes, multiple SPR typologies will be required, as different applications impose distinct thermal, chemical, and operational demands.

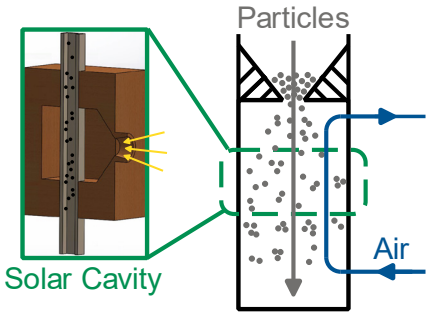

Figure 2: The concept of the CFDR consists of a falling particle stream in a tube, the falling speed of which is influenced by a counter-current air flow.

The indirectly irradiated CFDR consists of a tube that is enclosed by a solar cavity. High-temperature resistant particles are fed into the tube and fall by gravity through the irradiated section of the tube (see figure 2). While the particles pass through the tube, they take up heat via radiative heat exchange, as well as collisions with the interior of the tube. The novelty of this type of receiver is that a counter-current air flow can be introduced which slows down the falling speed of the particles.[11] Compared to scenarios without a counter-current air flow, this leads to higher particle outlet temperatures and higher thermal efficiencies. This approach of influencing the residence time of the particles in the receiver is relatively

simple and requires neither a pressurized gas flow nor complex rotation mechanics as is the case with fluidized bed receivers or rotary kiln receivers.

In recent years, gravity-driven particle solar receivers have gained increasing attention. Jiang et al.[12] investigated a dense particle-laden flow within a metallic tube, demonstrating wall-to-particle HTC exceeding $1000\ \mathrm{W\ m^{-2}K^{-1}}$. Martinek and Ma[13] introduced a light-trapping planar cavity receiver (LTPCR) design, utilizing a dense gravity-driven particle flow as the heat transfer medium. Experimental investigations demonstrated that wall-to-particle heat transfer coefficients of approximately $1000\ \mathrm{W\ m^{-2}K^{-1}}$ can be achieved.[14] The main distinction between these two concepts and the CFDR lies in the nature of the particle-laden flow, with the former employing a dense and therefore opaque flow, while the CFDR operates with a semi-opaque particle-laden flow. This allows radiation to penetrate deeper into the particle phase, which is believed to lead to a more volumetric heating of the particles.

Table 1 The three StoA SPR are compared with features of the CFDR concept. An advantage is marked with a green plus, a neutral point with a circle and a disadvantage with a red minus.

Particle Curtain Receiver		*Fluidized Bed Receiver*	
−	PRT can not be controlled	+	PRT can be controlled
+	Particle concentration can be controlled	O	Particle concentration not independent of carrier fluid rate
+	Stable operation, low OPEX	−	difficult to operate, high parasitic energy loss
+	Direct irradiation	±	Direct/ Indirect irradiation possible
−	Particle loss	+	No particle loss
−	Reaction Environment cannot be controlled	+	Reaction Environment can be controlled
Rotary Kiln Receiver		***Counter-Flow Downer Receiver***	
+	PRT can be controlled	+	PRT can be controlled
+	Particle concentration can be controlled	+	Particle concentration can be controlled
−	difficult to operate, high parasitic energy loss	O	compared to kiln/ fluidized receiver, the parasitic energy loss will be small
+	Direct irradiation	±	Direct/ Indirect irradiation possible
O	Loss of fine dust	+	No particle loss
−	Reaction Environment cannot be controlled	+	Reaction Environment can be controlled

1.2 Purpose of the Project

The goal of project REVERSO is to bring the concept of the CFDR from technology readiness level 2 (TRL2), i.e., the formulated technology concept, to TRL3, thus providing proof of concept. To this end, the formulated concept will be refined into a detailed design, fabricated, and the fluid dynamics as well as the thermal behaviour of the novel receiver will be investigated. With the knowledge gained, it will be possible to perform a comprehensive comparison with the three StoA typologies of SPR. In the end, proof of concept is evaluated on two key performance indicators (KPI):

a. Are wall-to-particles heat transfer coefficients (HTC) greater than $1000\ \mathrm{W\ m^{-2}\ K^{-1}}$ achieved?
b. Do the particle outlet temperatures exceed $1000\ °C$?

The CFDR is a particle-in-tube receiver concept like the fluidized bed receiver. For the CFDR to be a valuable addition to the range of SPR, it is important that the wall-to-particles HTC are at least as high as for the fluidized bed receiver, which were experimentally determined to range from 300 to well above $1000\ \mathrm{W\ m^{-2}\ K^{-1}}$.[15,16] Achieving particle outlet temperatures exceeding $1000\ °C$ is desirable for several reasons: (a) enabling more cost-effective TES, (b) providing high-temperature process heat for

industries like the cement production, (c) running a high-temperature supercritical CO_2 Brayton Cycle which is more efficient than the current Rankine Cycle used for electricity generation, and (d) allowing to exploit thermochemical process routes for the synthesis of chemicals such as drop-in fuels or hydrogen.[9,17–20]

Comparing the CFDR with other concepts such as the fluidized bed receiver[15] or a similar concept by Jiang et al.,[12] this receiver contains a ceramic tube instead of a metal tube, which makes it possible to test for particle outlet temperatures exceeding $1000\,°C$.

1.3 Objectives

Project REVERSO has the following objectives:

a. Development of the formulated CFDR concept into a production-ready design, which includes the dimensioning of the individual components and the creation of a CAD model of the receiver.

b. Fabrication of the CFDR.

c. Fundamental investigation of the fluid dynamics as well as the thermal behaviour of the novel receiver. To better understand the thermal behaviour, it is planned to support the experimental study by developing a first-order heat transfer model.

d. Comparing the novel receiver with the three StoA typologies of SPR and evaluating the two KPIs.

2 Description of Facilities

2.1 The Counter-Flow Downer Receiver

The CFDR was designed to fit in the high-flux solar simulator allowing for as much space for the particle-laden flow to develop, and at the same time enough room for the particle feed and collection system. Each component that forms the CFDR is manufactured from numerous (mostly) off-the shelf items, sometimes limiting the choice on the final dimensions of individual parts. The receiver consists of a silicon carbide (SiC) tube that is enclosed by a solar cavity. The solar cavity is made out of insulation bricks (Altraform KVS 184/400) that are housed in a stainless steel shell, and contains a 40 mm diameter circular aperture for the access of concentrated solar radiation. Ceramic particles are supplied to the tube from the top via a hopper, whose outlet opening is controlled by an automatic knife gate valve. The particles fall by gravity through the irradiated SiC tube and are collected in a container, whose weight is continuously monitored. Air at ambient pressure is fed to the tube from the bottom at a controlled flow rate and flows upwards, counter current to the fall direction of the particles. A schematic of the SPR can be seen in figure 3.

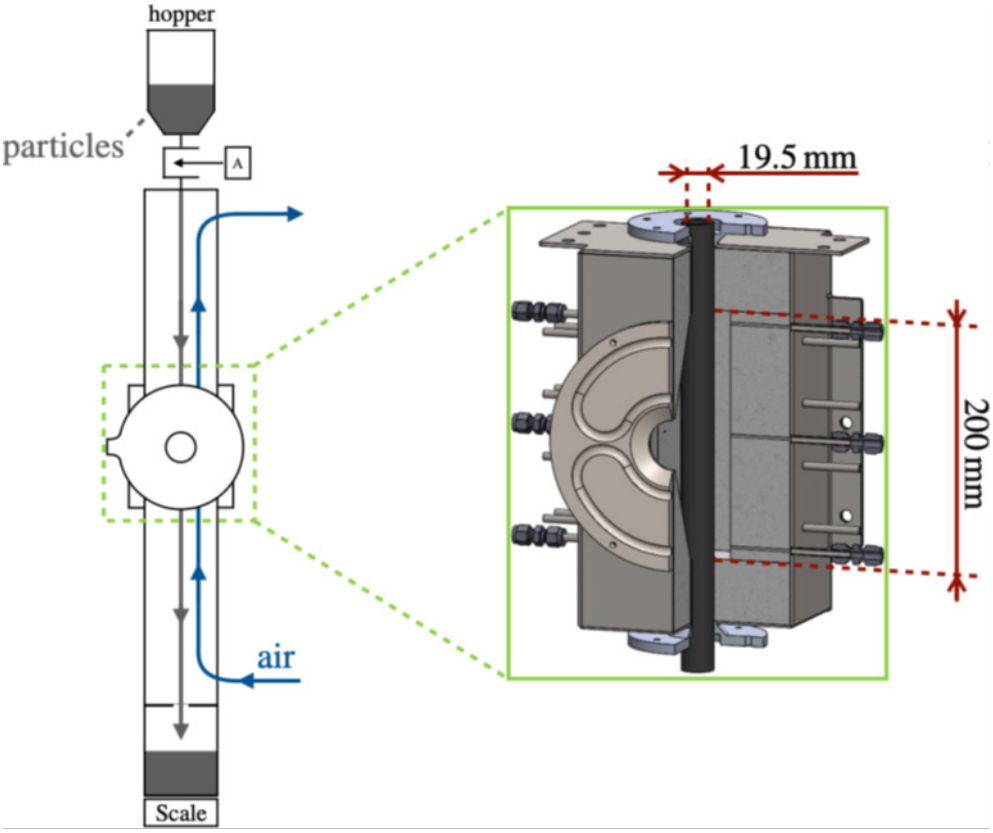

Figure 3: On the left-hand side, a schematic of the CFDR is shown. On the right-hand side, a detailed computer-aided design (CAD) of the solar cavity enclosing the SiC tube is given. The interior of the solar cavity consists of Altraform KVS 184/400 insulating bricks arranged in a stainless steel shell. In the front, the cavity is protected by a radiation shield made out of aluminium, which has an aperture of 40mm.

The ceramic particles used are made from the material CARBOBEAD HTM ID (CARBO Ceramics Inc.), which consists to 70-80 % of alumina oxide, 10-20 % of silicon oxide and the remainder of iron oxide and titanium oxide. These particles were selected due to their temperature resistance, good flowability, high thermophysical properties, as well as high absorptance.[21] Particles made out of this material are used in several studies around CSP, especially for particle curtain receivers.[9,22] In general, the range of acceptable particle diameters depends on processability and the desire for a high heat transfer. With

regard to heat transfer, a smaller particle diameter is desirable as the specific surface area is increased, which leads to an increase in heat transfer. However, the smaller the particles are, the more difficult they are to handle due to static effects. Initially, the particle size distribution (PSD) showed a significant number of particles with a diameter lager than 300 µm. To limit the number of particles with such large diameters, they were sieved using sieves with a mesh size of 200 µm, and 250 µm. Figure 4 shows the resulting PSD of the particle population used during the irradiation campaign.

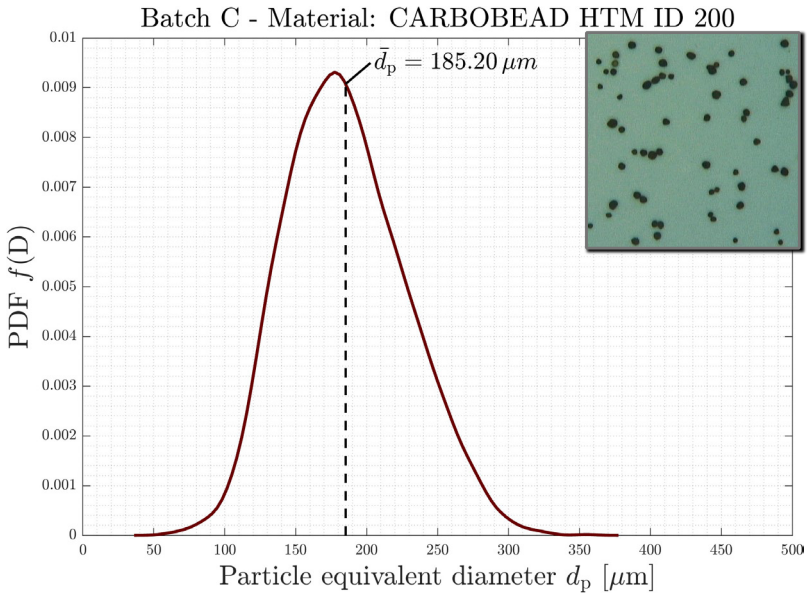

Figure 4: The PSD of the particle population used during the irradiation campaign has a mean particle diameter of around 185 µm with a good cut-off for particles with a diameter less than 50 µm or more than 300 µm. A raw image of the particles can be seen in the right upper corner.

2.2 Research Facilities

EFD Laboratory at ETH Zurich, Switzerland

A prototype of the CFDR made from materials allowing for visual access was built and placed inside the laboratory of the experimental fluid dynamics group (EFD) at ETH.

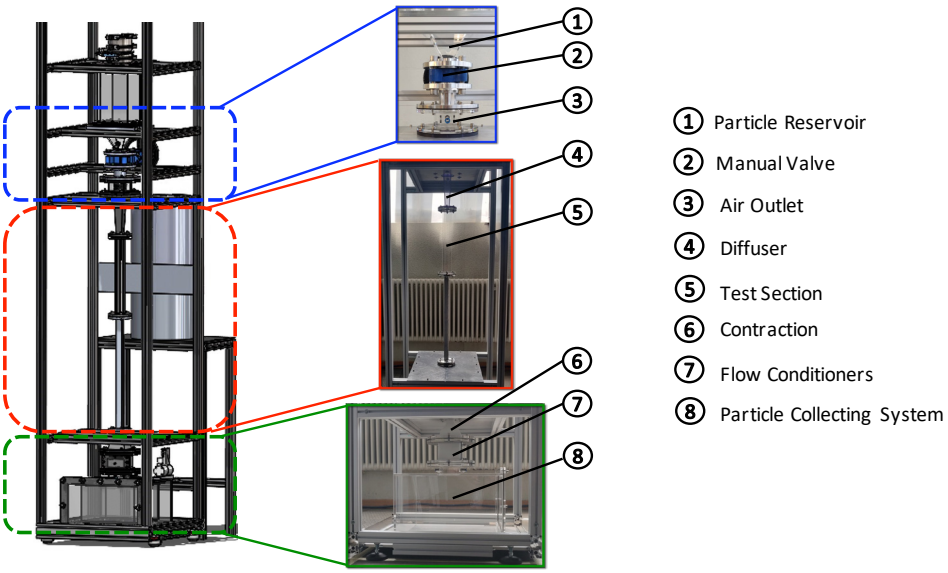

Figure 5: On the left-hand side the CAD of the prototype is given. The pictures in the middle show parts of the prototype, which is in the EFD laboratories. A description of the parts is given on the right-hand side.

The laboratory of EFD offers the infrastructure to validate the derived concept of the CFDR and to investigate its fluid dynamics in detail via high-speed imaging. In figure 5 a description of the prototype can be found. In general, the system can be considered a “vertical wind tunnel” as it contains a flow conditioning section, a contraction section, and a diffuser section. The fluid as well as particle mass flow rate can be tuned individually via the mass flow controller (MFC), manual knife gate valve respectively. Compared to the final version of the CFDR, a square channel ($20\,\mathrm{mm} \times 20\,\mathrm{mm}$) was used as the test section instead of a tube. The reason for this is that it allows for an easier imaging of the particle-laden flow.

PREC Laboratory at ETH Zurich, Switzerland

Just like the prototype, the final setup can be seen like a vertical wind tunnel containing flow conditioners, a contraction, as well as a diffusor section (see figure 6). However, instead of a square inner geometry, all pieces have a circular inner geometry, whereby the characteristic length was kept the same between the two facilities. In general, all parts that are not in the vicinity of the irradiated solar cavity or the heated particles are made of stainless steel. Parts that are irradiated by the high-flux solar simulator (HFSS) or in direct contact with the heated particle-laden flow are made of an insulating material that is commonly used in sintering furnaces (Altraform KVS 184/400). The density of the insulating material is relatively low, making it necessary to protect those parts in stainless steel shells.

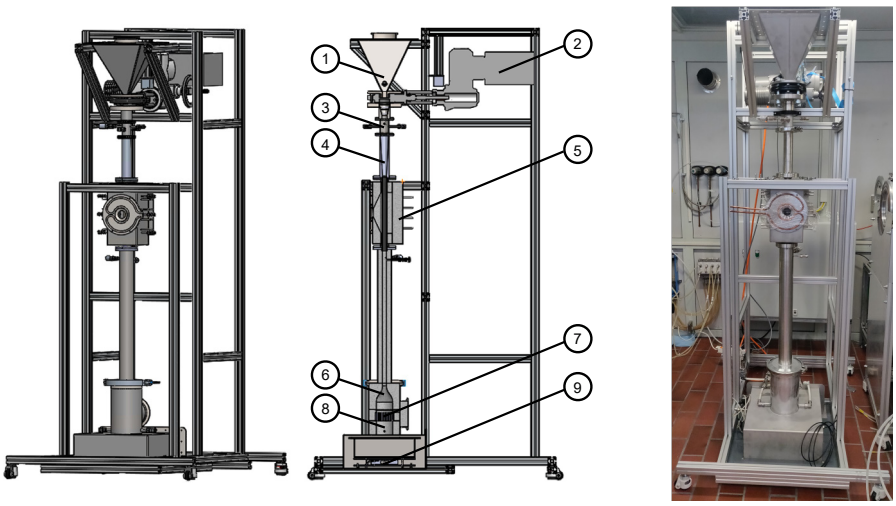

Figure 6: The CAD of the CFDR is shown, as well as a section view of it. Similar to the prototype, the receiver is built out of the components: (1) a particle reservoir/ hopper, (2) an automatic knife gate valve, (3) an air outlet, (4) a diffuser, (5) the solar cavity containing the SiC duct, (6) a contraction, (7) flow conditioners and (8) a particle collecting system. Additionally, a picture of the final assembly is shown.

To investigate the thermal performance of the CFDR, the setup was placed in one of the HFSS in the Professorship of Renewable Energy Carriers (PREC) laboratory (see figure 7). The HFSS consists of seven high-pressure xenon arcs, each surrounded by an ellipsoidal reflector, which produce radiation with similar qualities than our sun. The lamps can be operated independently allowing to perform experiments with varying power inputs $\dot{Q}_{\mathrm{solar}}$ and concentration ratios C, which is an indicator of how much of the initial irradiation falling on the solar collector system is concentrated on the solar receiver

$$C = \frac{\dot{Q}_{\mathrm{solar}} / A_{\mathrm{aperture}}}{I_{\mathrm{DN}}} = \frac{\dot{q}_{\mathrm{in}}}{I_{\mathrm{DN}}}$$

with $\dot{q}_{\mathrm{in}}$ being the heat flux on the aperture of the solar cavity and I_{DN} the direct normalized irradiance which is often assumed to be 1 kW m^{-2} representing peak solar conditions.

Figure 7: A HFSS mimics the behaviour of concentrating solar systems and is used as radiation source during the irradiation tests. The aperture location is determined by the point where the radiation from each lamp is focused on (as indicated by the yellow cone). An image of the installation is given on the right-hand side.

3 Procedures and Methodology

3.1 Fabrication of the CFDR

To allow for more flexibility, it was decided to build two versions of the CFDR. The first one, called prototype or cold set-up, is used to test the functionality of the derived CFDR concept and investigate its fluid dynamics. The second version of the CFDR, referred to as hot set-up, was built to investigate the thermal performance of the receiver and is made from high-temperature resistant materials. Both setups consist of the same components, however, it was necessary to work with two different inner geometries. The prototype has a square inner geometry allowing for easier imaging through the flat wall of the test section. For the final version, it was necessary to work with a circular inner geometry resulting in a better heat distribution inside each component. A detailed description of the two newly constructed facilities can be found in section 2.

3.2 Experimental Assessment

Fluid Dynamic Study

A 2D high-speed imaging set-up consisting of a high-speed camera (Phantom VEO 640L) equipped with a 50 mm lens (Zeiss Milvus 1.4/50 ZF.2-mount) and a LED backlight is used to investigate the particle-laden flow inside the transparent test section (see figure 8). A field of view of approximately 214 mm x 21 mm (*z*-*x* plane) is sampled, and images are acquired at a frequency of 4000 Hz, resulting in a maximum particle shift between consecutive images of around 8 pixels. Particle Image Velocimetry (PIV) is used to obtain 2D instantaneous velocity profiles and concentration profiles of the particle phase. Due to the nature of the imaging setup employed, it is assumed that the 2D PIV data is spatially averaged along the *y*-coordinate. The velocity profiles are used to compare the spatiotemporal averaged fall speed of the particle phase between experiments with and without the counter-current air flow. Finally, a flow map is created containing the parameter space air mass flow versus particle volume concentration, which provides an indication of certain flow conditions, such as a laminar or turbulent particle-laden flow.

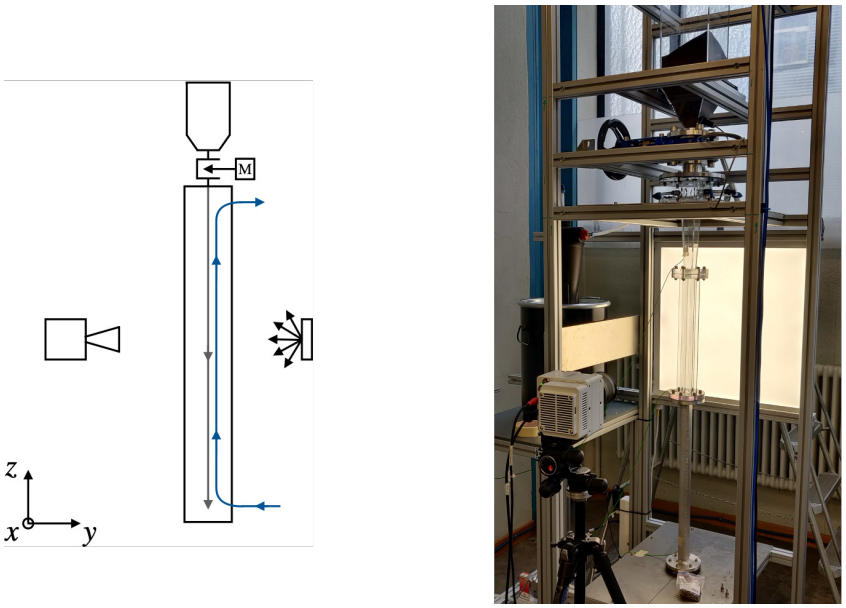

Figure 8: A simplified sketch of the imaging setup is shown, as well as a picture of the experimental arrangement.

Calorimetry: Measuring the Radiant Power Provided by the HFSS

A water-cooled calorimeter, placed on a translation stage that allows the calorimeter to be moved in all three dimensions, is used to determine the radiant power provided by the HFSS, $\dot{Q}_{\mathrm{solar}}$ (see figure 9). Measuring the water flow rate and the water inlet and outlet temperature in the calorimeter enables the determination of $\dot{Q}_{\mathrm{solar}}$ via the enthalpy change in the water phase

$$\dot{Q}_{\mathrm{solar}}\,[\mathrm{W}] = \dot{V}_{\mathrm{H_2O}}\varphi_{\mathrm{H_2O}}\left[\mathrm{h}^{\mathrm{out}}_{\mathrm{H_2O}}\left(T^{\mathrm{out}}_{\mathrm{H_2O}}\right) - \mathrm{h}^{\mathrm{in}}_{\mathrm{H_2O}}\left(T^{\mathrm{in}}_{\mathrm{H_2O}}\right)\right] \tag{1}$$

with ρ_{H2O} being the density of water, $\mathrm{h}^{\mathrm{in}}_{\mathrm{H_2O}}$ being the specific enthalpy of the water phase at the inlet of the calorimeter and $\mathrm{h}^{\mathrm{in}}_{\mathrm{H_2O}}$ being the specific enthalpy of the water phase after leaving the calorimeter.

Initially, the translation stage is used to find the location where the maximum power input $\dot{Q}_{\mathrm{solar}}$ is measured. This location is the point where the second focal points of the truncated elliptical concentrators surrounding the xenon lamps meet. Once found, the calorimeter is fixed in space and $\dot{Q}_{\mathrm{solar}}$ measured for different lamp configurations. An important detail is that the diameter of the aperture of the calorimeter matches that of the CFDR, as this determines how much of the light cone coming from the HFSS can enter the cavity and how much radiation can be reradiated from the cavity into the environment. Both the calorimeter and the solar cavity of the CFDR have an aperture of 40mm, so it can be assumed that $\dot{Q}_{\mathrm{solar}}$ is the same during the irradiation tests.

Figure 9: An image of the calorimeter setup is shown. The red oval highlights the front of the calorimeter, which is facing the HFSS.

Thermal Behaviour

The HFSS is used to conduct a campaign of irradiation tests studying the thermal performance of the CFDR. During the irradiation tests, the temperature of the solar cavity, SiC tube, as well as the particle-laden flow will be monitored with thermocouples (TCs). The TCs are located at varies heights such that the temperature profiles can be resolved in time and space (see figure 10). A priori, it cannot be ruled out that the high radiation environment inside the SiC tube influences the temperature reading of the particle-laden flow. Therefore, an arrangement of two TCs, each with a different bead diameter, is installed so that a possible influence on the measurement can be detected.[23] The temperature profiles are used to compute the thermal efficiency η_{th}, and the local heat transfer coefficient h at the location z = 0.98 m using Newton's cooling law and assuming the system is in thermal equilibrium.

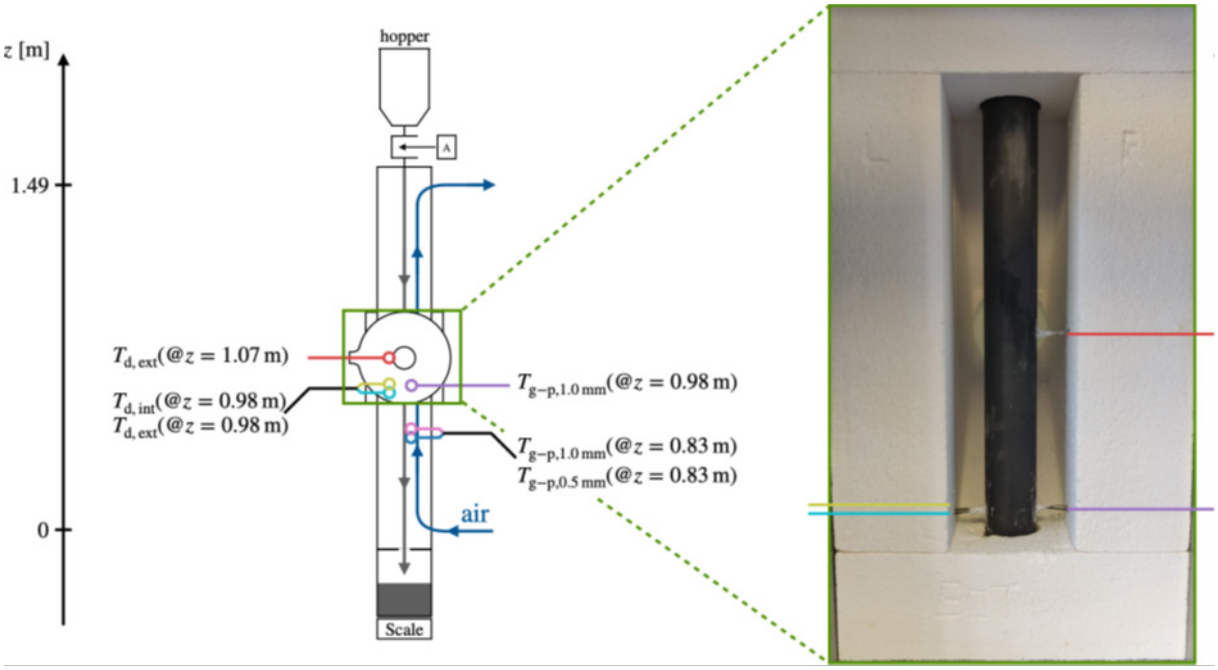

Figure 10 Highlighted are key TCs positions that are used to measure the temperature of the particle laden flow T_{g-p}, the external wall temperature of the SiC tube $T_{d,ext}$, as well as the internal wall temperature of the SiC tube $T_{d,int}$. If needed, the diameter of the TC bead is indicated in the subscript. The image inside the green box shows the TC arrangement around the SiC tube. High-temperature resistant cement was used to secure the tips of the TCs on the tube.

3.3 Simulations

A simulation of the CFDR is developed, consisting of a one-dimensional first-order heat transfer model of the particle-laden flow inside the SiC tube, a three-dimensional heat transfer model to predict the surface temperatures inside the solar cavity, and an in-house software to simulate the incoming radiation generated by the HFSS. A priori, the amount of heat extracted by the particle-laden flow is unknown, which is why the heat transfer problem must be solved iteratively. The flow sheet in figure 11 presents the computational steps taken to solve for a converged solution of the simulation.

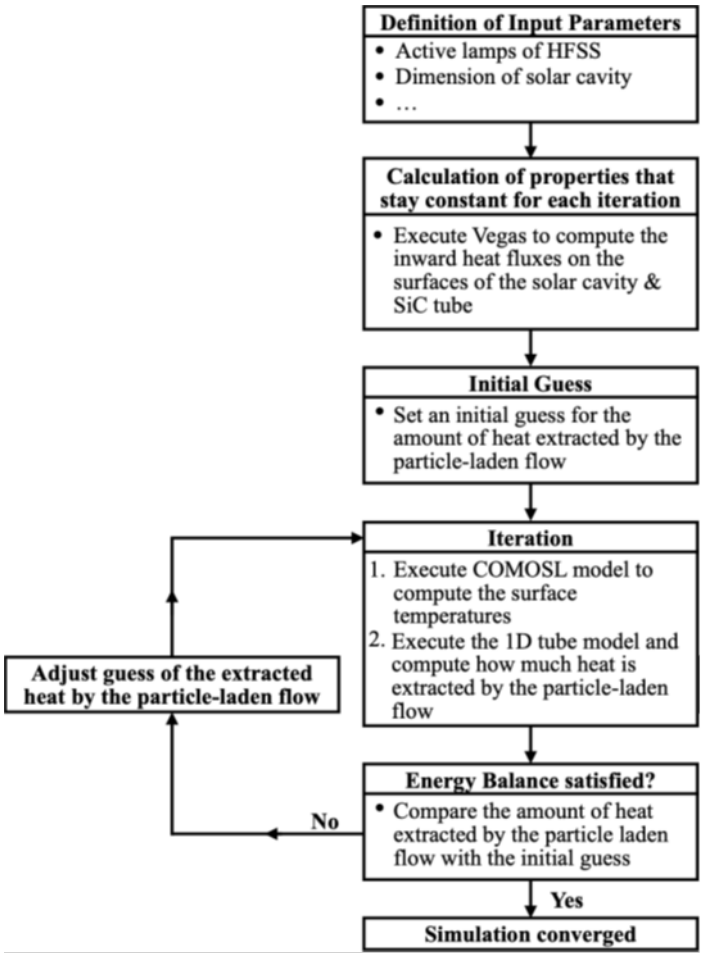

Figure 11: The high-level flow sheet shows how the three different elements of the simulation are connected and how a converged simulation results is obtained.

The project will be concluded with a comparison of the simulation data with the experimental data. If the simulations and experiments agree to a reasonable extent, it will be possible to perform an evaluation of the projected levelized cost of energy (LCOE) for a scaled-up version of the receiver.

Monte Carlo Ray-Tracing

It is important to capture the correct geometry of the light cone being produced by the HFSS that is entering the aperture of the solar cavity. Therefore, an in-house 3D Monte-Carlo Ray Tracing (MCRT) tool called Vegas is used to capture the radiation coming from the HFSS as precise as possible.[24]

3D Heat Transfer Simulation of Solar Cavity

A three-dimensional heat transfer model of the solar receiver was developed using COMSOL Multiphysics v6.2. At first, the model was used to gain an understanding of how the placement of the tube, the thickness of the insulation, the size of the opening and the geometry of the solar cavity affect the thermal efficiency of the solar receiver. Now, the 3D heat transfer model is updated to the manufactured geometry of the experimentally tested solar cavity and coupled to the results of the MCRT. In a next step the first-order numerical simulation of the particle-laden flow inside the tube will be coupled as well.

First-Order Numerical Simulation of the Particle-Laden Flow Inside the Tube

The simulation of the tube allows to investigate the main heat transfer phenomena driving the heat exchange between the tube walls and the particle-laden flow. The focus is on the heat transfer modes convection and radiation, as it is assumed that they are the main driving forces for heat exchange in the tube.

4 Progress Report & Results

4.1 Fabrication of the CFDR

Both setups, the transparent prototype as well as the final version of the solar particle receiver were successfully designed, produced and installed. Both facilities operate as intended and are used to investigate the CFDR.

4.2 Fluid Dynamic Study of the CFDR

The goal of this analysis was to investigate, if the presence of the counter-current air flow decreases the averaged fall speed of the particle phase compared to a case without the air flow being present. Therefore, the focus is on the instantaneous velocity profiles of the downward velocity component $w(x,z)$. In general, the solid volume fraction was kept constant and the amount of counter-current air flow increased from no air to up to $\dot{V}_f = 20\,\mathrm{ln\,min^{-1}}$. Multiple image sets for varying particle mass flow rates $\dot{m}_s \in [3.7,\ 101.2]\ \mathrm{g\ s^{-1}}$ and air flow rates $\dot{V}_f \in [0,\ 20]\ \mathrm{ln\,min^{-1}}$ were taken. An overview of the data sets taken can be found in figure 12.

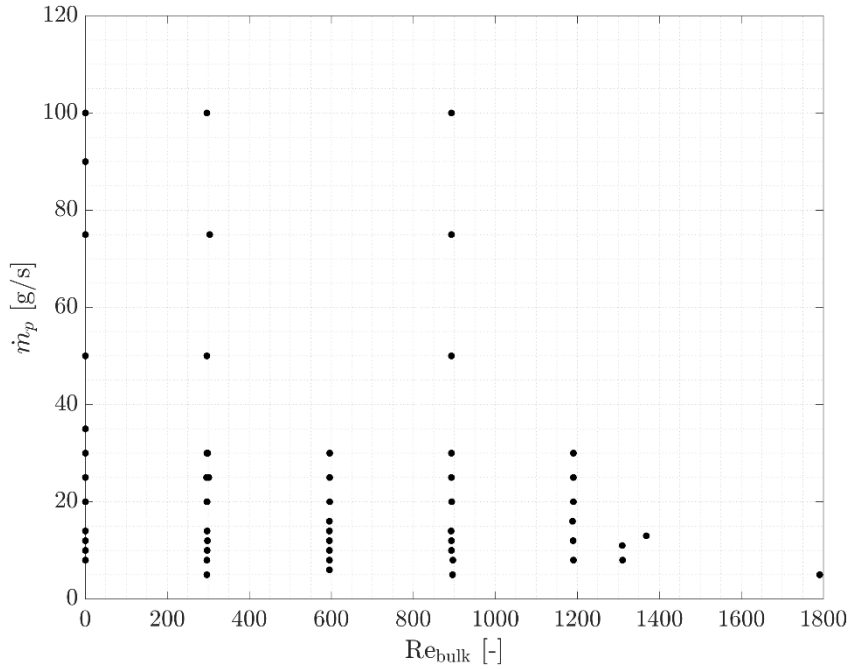

Figure 12: The graphic shows an overview of the image sets recorded for different combinations of particle mass flow and air flow. Data sets below the red line could be processed with a standard PIV scheme. For the data sets above the red line PIV was not an option, because of the high opaqueness of the flow.

Figure 13 contains a selection of images showcasing qualitatively, how the nature of the particle-laden flow changes when the solid volume fraction $\phi_{v,s}$ is increased. For small $\phi_{v,s}$ the particles fall in a laminar manner, once $\phi_{v,s}$ is increased, darker regions appear indicating that the particles start to cluster in certain regions of the flow.

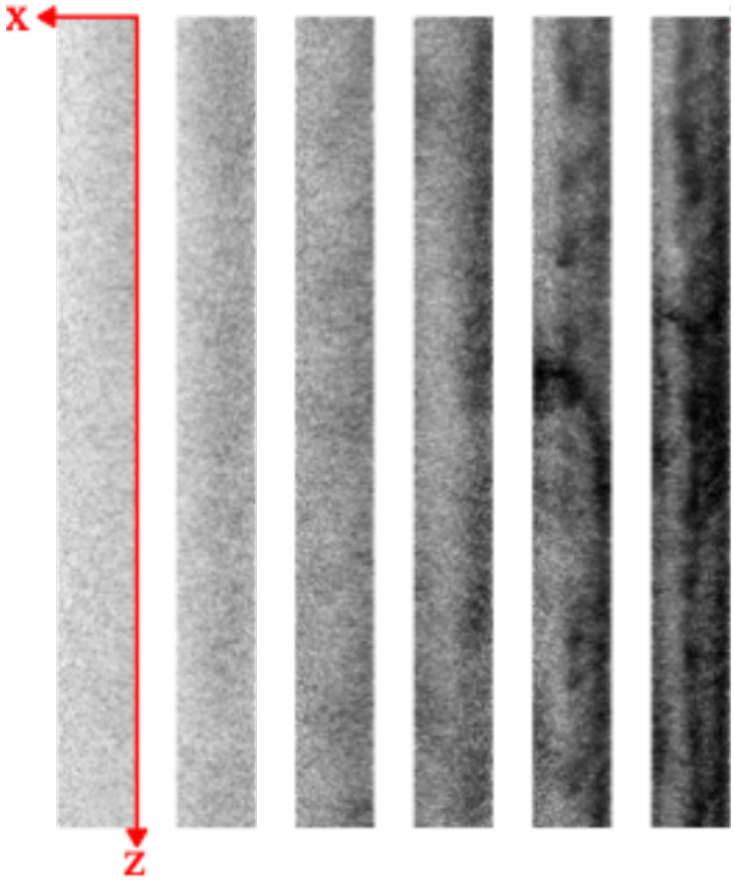

Figure 13: Images of the particle-laden flow inside the square duct of the transparent prototype are shown. The solid volume fraction $\phi_{v,s}$ increases from the left side to the right side $\phi_{v,s} \in \{0.26, 0.46, 0.67, 0.87, 1.06, 1.26\}\%$. The coordinate system is indicated by the red arrows.

The image sets were processed using PIVlab[25] yielding the instantaneous velocity profiles. Up to a solid volume concentration of $\phi_{v,s}$ = 1.26%, the PIV algorithm worked well in identifying corresponding structures between consecutive images. For higher solid volume fractions, the successful detection of coherent flow structures decreased leading to a reduced quality of the instantaneous velocity profiles. Therefore, it was decided to focus on the data sets that could be analyzed with the conventional PIV approach and to work on an adapted image processing approach for the cases with higher solid volume fraction in the future. The so far unprocessed data sets do not correspond to flow regimes that were investigated during the irradiation test campaign, due to the fact that the HFSS does not provide enough power input to investigate such high particle mass flow rates.

Table 2 Given are the velocity ratios VR computed for the two cases of constant solid volume fraction and varying air flow rate from no air to up to $\mathbf{20\,ln\,min^{-1}}$. A decrease in the velocity ratio corresponds to a decrease in the average fall speed.

Re_{bulk}	VR for $\phi_{v,s} \approx 4.6 \times 10^{-3}$ [%]	VR for $\phi_{v,s} \approx 9.0 \times 10^{-3}$ [%]
0	100	100
293	54	42
595	46	39
893	38	33
1190	-	25

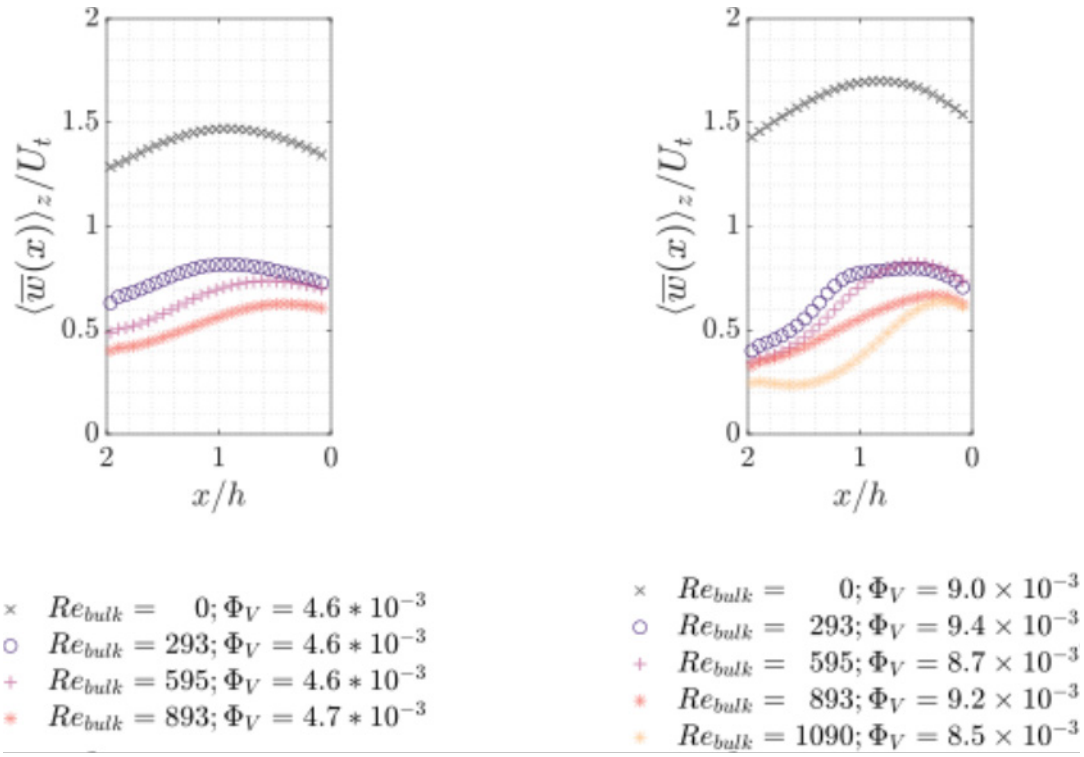

Figure 14: The temporally averaged vertical velocity component profiles, averaged over the *z*-component are shown for two constant solid volume fractions and varying air flow rates. For both cases, the average fall speed of the solid phase decreases when increasing the air flow rate. The velocity profiles were measured inside the transparent prototype.

In figure 14, the influence of a varying counter-current air flow on the average fall speed of the particle phase is compared for two different solid volume fractions. For both solid volume fractions, once the counter-current air flow is present, the average fall speed is drastically reduced. A further increase in the air flow rate leads to a further reduction in the average fall velocity. The velocity ratio VR was defined

$$\mathrm{VR} = \frac{\langle \overline{w} \rangle_{x,z}\left(\dot{V}_f > 0 \,\mathrm{ln\,min^{-1}}\right)}{\langle \overline{w} \rangle_{x,z}\left(\dot{V}_f = 0 \,\mathrm{ln\,min^{-1}}\right)} \quad \text{for. } \phi_{\mathrm{v,s}} \approx \text{const.} \tag{2}$$

to quantify the percentage reduction in average fall speed relative to the scenario without air. Without air, the fall speed is at its highest (VR =100 %), as soon as a certain air flow rate is set, the fall speed drops to a fraction of this. For example, $\phi_{\mathrm{v,s}} \approx 9 \times 10^{-3}$ and $\mathrm{Re_{bulk}} = 1190$, the fall speed drops to only 25% of the fall speed for the scenario without air.

4.3 Simulation of the CFDR

Progress on all three parts of the simulation were made. The geometry of the final solar cavity was implemented in Vegas, as well as COMSOL, and the 1D model of the particle-laden flow was adjusted to account for the change from a square duct to a tube (see figure 15). The results of the MCRT simulation are coupled with the 3D heat transfer model via heat flux boundary conditions on the inner surfaces of the solar cavity and the SiC tube. In a next step, the COMSOL model is adjusted such that surface-to-surface radiation is considered and the 1D heat transfer model coupled to the COMSOL model including the iterative procedure to obtain a converged solution of the simulation.

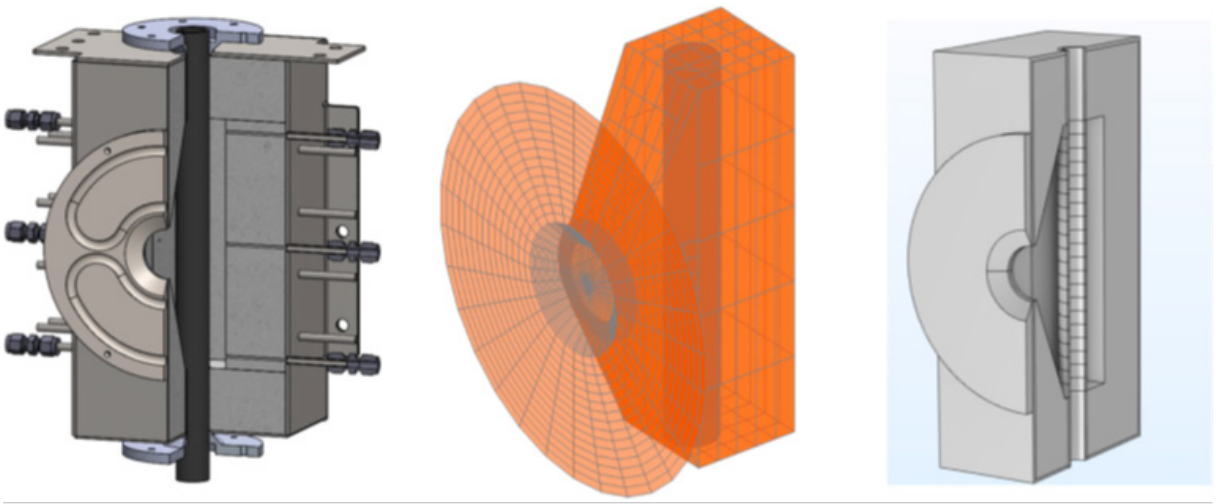

Figure 15: The CAD of the solar cavity is shown on the left. The image in the middle illustrates how the inner surfaces of the cavity are discretized in Vegas and the image on the right shows how the solar cavity is implemented in COMSOL.

4.4 Calorimetry: Measuring the Radiant Power Provided by the HFSS

The radiant power input was determined for two different lamp configurations: (a) 5 lamps (Arc 1,2 & 5-7), and 6 lamps (Arc 1-3 & 5-7, see figure 7 for numbering of Arcs). Figure 16 shows the measured water temperatures, water flow rate and the corresponding power input while using 6 lamps at full capacity. The water flow rate was measured before entering the calorimeter which is why the density $\rho_{H_2O}(@T = T^{in}_{H_2O})$ was used to compute the water mass flow rate $\dot{m}_{H_2O(l)}$.

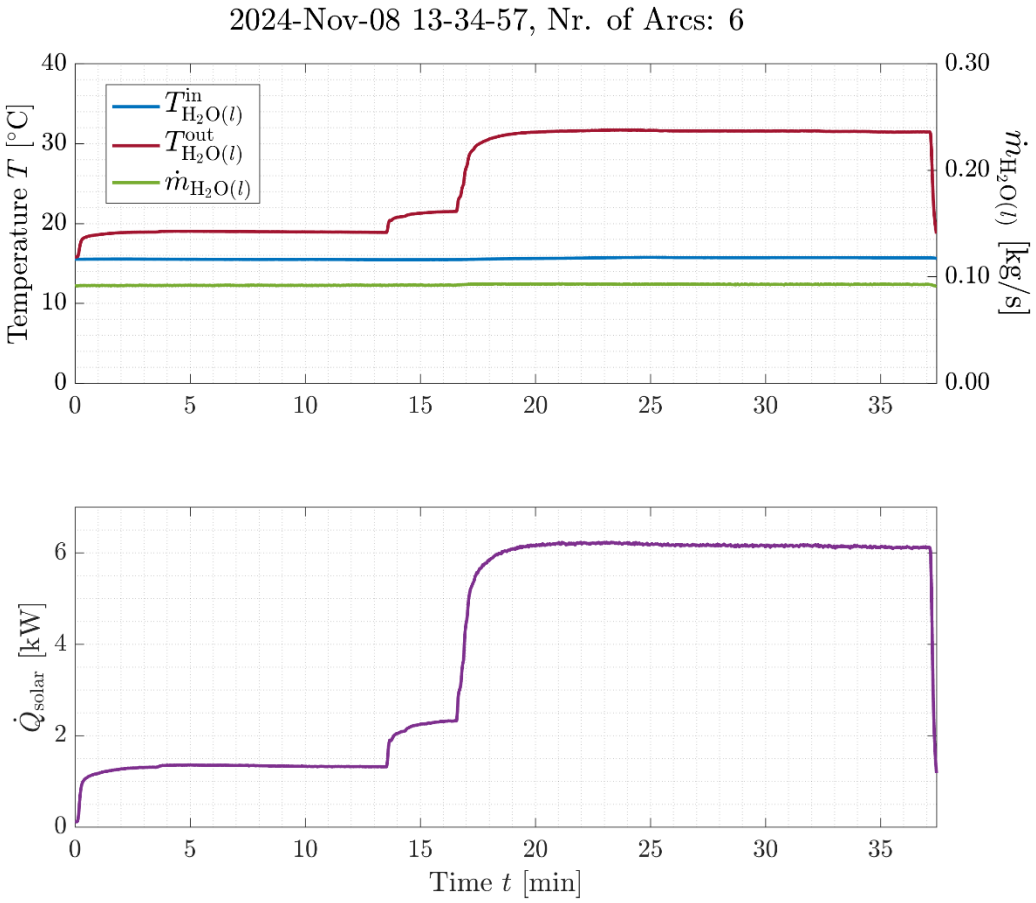

Figure 16 The calorimetry measurement for a lamp configuration of 6 lamps is shown. In average, a radiant power input of $\boldsymbol{Q_{solar}}$ = 6.21kW was measured.

In the end, the following radiant power inputs $\dot{Q}_{solar}$ were measured

configuration (a):	5 lamps (Arc 1,2 & 5-7)	$\dot{Q}_{solar}$ = 5.36 kW
configuration (b):	6 lamps (Arc 1-3 & 5-7)	$\dot{Q}_{solar}$ = 6.21 kW

4.5 Thermal Assessment of the CFDR

Representative for all irradiation tests, figure 17 contains an example of a temperature profile measured for a fixed particle mass flow rate and counter-current air flow rate. For each test case, the solar receiver was pre-heated for around 80 minutes, which led to a quasi-steady state temperature profile inside the solar cavity. Then, the particle mass flow rate, as well as the desired air flow rate were set. Afterwards, the system was given enough time to equilibrate to the new quasi-steady state.

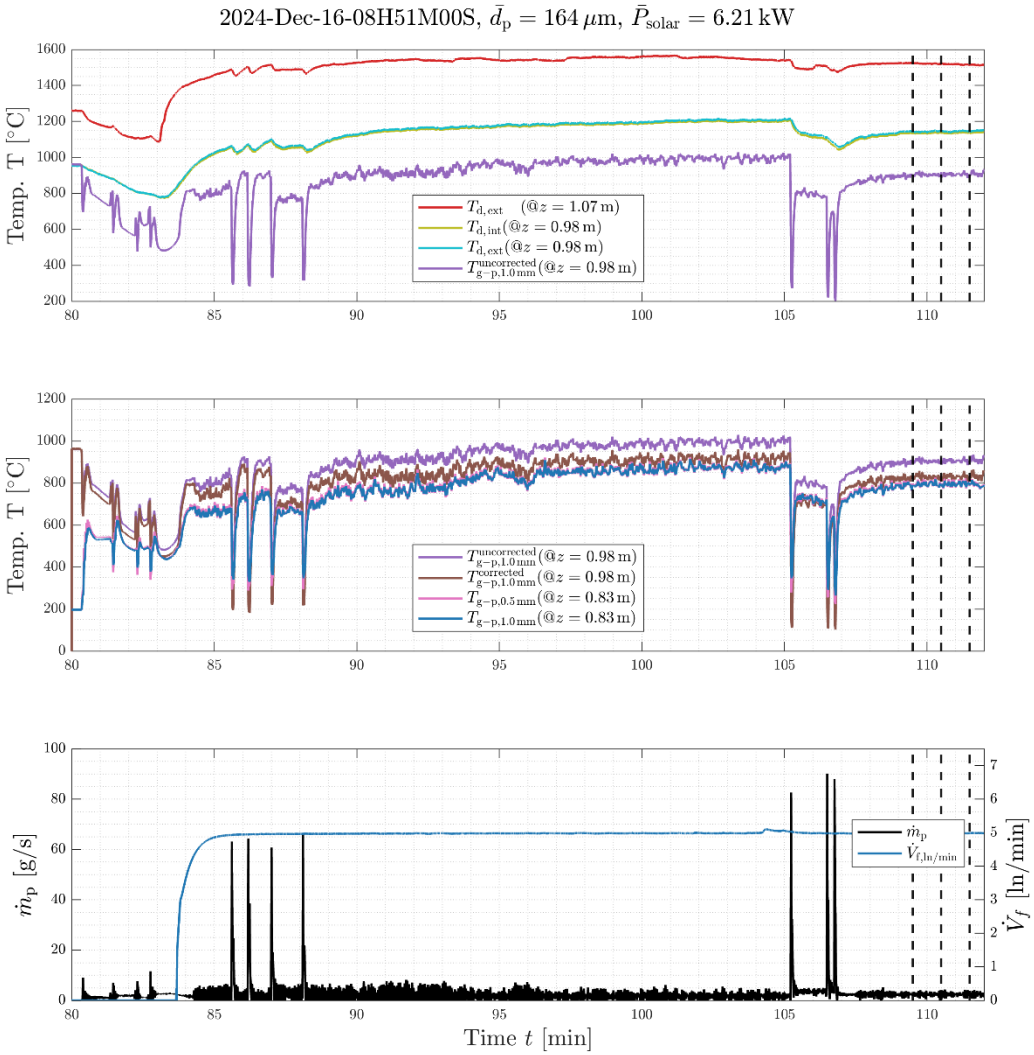

Figure 17: The first figure shows the temperature profile of the external wall temperature of the SiC tube at two different locations, $T_{d,ext}(@z)$, one internal wall temperature profile of the SiC tube, $T_{d,int}(@z)$, as well as the temperature measurement of the particle-laden flow at the outlet of the SiC tube, $T_{g-p}^{uncorrected}(@\,z = 0.98\text{ m})$. In the second figure, the temperature reading of the particle-laden flow at the outlet of the SiC tube, $T_{g-p}^{uncorrected}(@\,z = 0.98\text{ m})$, and below the solar cavity, $T_{g-p}(@\,z = 0.83\text{ m})$, is shown (location of TCs see figure 10).The last figure contains the air flow rate $\dot{V}_f$, as well as the particle mass flow rate $\dot{m}_s$ over time. The data was acquired using the setup located in the PREC laboratory (see section 2).

Due to the intermittent nature of the temperature profiles, the temperatures that are going to be reported are always temporal averages over at least one minute of temperature readings measured during the new quasi-steady state. The averaging intervals are indicated by the black dashed vertical lines in the figure. As expected, the measurement of the external wall temperature in the center of the SiC tube was the highest, followed by the temperature measurement of the external and internal wall temperature of the SiC tube near the bottom of the solar cavity. Also, the temperature reading of the particle laden flow

is higher at the outlet of the SiC tube compared to the temperature reading taken slightly below the solar receiver at a height of roughly $z = 0.83$ m. The two-TCs probe data revealed that the temperature measurements at a height of 0.98 m are influenced by the radiation coming from the surrounding and therefore only the temperature measurements at a height of 0.83 m were considered for the analysis of the thermal efficiency and the local wall-to-particles HTC.

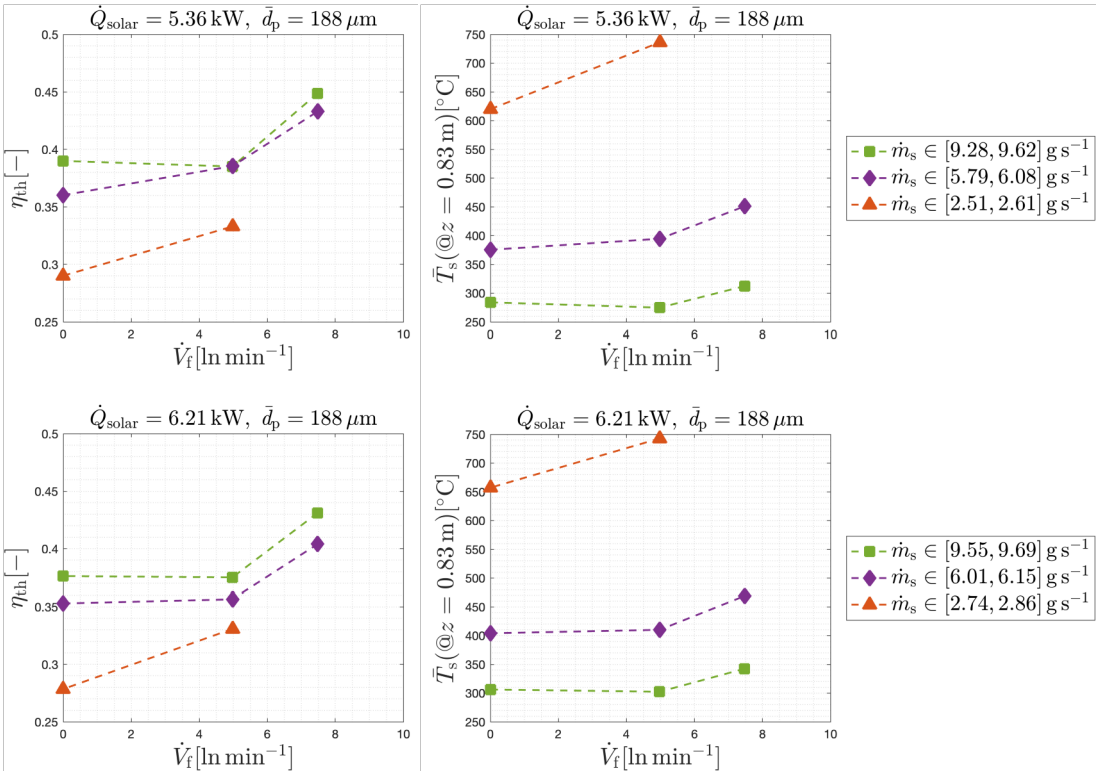

Figure 18: Each row of figures contains data taken with the same power input $\dot{Q}_{\mathrm{solar}}$. Cases with comparable particle mass flow rates are grouped together so that it is possible to assess how the presence of the counter-current air flow affects the thermal efficiency as well as the average outlet temperature of the particle-laden flow. For all data points the same population of particles were used which had a mean diameter of around 188 µm.

The thermal efficiency of a solar receiver is defined by the quotient of the heat transferred to the HTM over the radiative heat supplied by the radiation source. For the presented receiver follows

$$\eta_{\mathrm{th}} = \frac{\dot{m}_s c_{p,s}\left[T_s^{\mathrm{out}} - T_s^{\mathrm{in}}\right]}{\dot{Q}_{\mathrm{solar}}} \tag{3}$$

with $c_{\mathrm{p,s}}$ being the isobaric specific heat capacity of the particles, T_s^{out} being the particle temperature $@z = 0.83$ m and T_s^{in} being the temperature of the particles inside the hopper, which was assumed to be 25 °C. Only the heat absorbed by the particle phase is considered, as the heat absorbed by the air phase accounts for less than 5 %.[26]

Figure 18 presents the thermal efficiencies that were computed with the temperature data $@z = 0.83$ m with respect to different air flow rates. Each row contains data sets that were measured with the same radiative power input $\dot{Q}_{\mathrm{solar}} \in \{5.36, 6.21\}$ kW. The data is grouped by comparable particle mass flow rates: (a) square shape - $\dot{m}_s$ around 9.5 g s^{-1}, (b) diamond shape - $\dot{m}_s$ around 6 g s^{-1} and (c) triangle shape - $\dot{m}_s$ around 2.6 g s^{-1}. All data points were measured with the same particle population that had a mean particle diameter of around 185 µm. For higher particle mass flow rates, the presence of the counter-current air flow alone does not lead to a significant increase in the thermal efficiencies. However,

once the air flow rate is set high enough a substantial increase of η_{th} could be measured. Further, the presence of the counter-current air flow leads to an increase in the average outlet temperature of the particle-laden flow, as summarized in table 3. To achieve higher particle outlet temperatures, the overall temperature of the solar cavity must be increased. However, as the cavity temperature rises, re-radiation losses also increase, resulting in the observed trend of decreasing thermal efficiencies at higher particle outlet temperatures. This trend is well known in literature, as the radiative losses scale with the fourth power of the cavity temperature.[27,28]

Table 3 The numerical values of the particle mass flow rate, the air flow rate, the thermal efficiency, as well as the average outlet temperature of the particles at the location $z = 0.83$ m are here summarized. For each table, the experiments were performed with the same power input $\boldsymbol{Q_{solar}}$.

(a) $\dot{Q}_{solar} = 5.36\,\mathrm{kW}$				**(b)** $\dot{Q}_{solar} = 6.21\,\mathrm{kW}$			
$\dot{m}_s$ $[\mathrm{g\,s^{-1}}]$	$\dot{V}_f$ $[\mathrm{ln\,min^{-1}}]$	η_{th} $[-]$	$\bar{T}_s(@z = 0.83\,\mathrm{m})$ $[°\mathrm{C}]$	$\dot{m}_s$ $[\mathrm{g\,s^{-1}}]$	$\dot{V}_f$ $[\mathrm{ln\,min^{-1}}]$	η_{th} $[-]$	$\bar{T}_s(@z = 0.83\,\mathrm{m})$ $[°\mathrm{C}]$
9.28	0.00	38.99	284.0	9.55	0.00	37.62	306.3
9.50	4.98	38.51	275.7	9.65	4.97	37.51	302.4
9.61	7.48	44.87	312.3	9.69	7.47	43.09	342.4
6.08	0.00	36.02	375.4	6.15	0.00	35.39	404.1
5.95	4.98	38.55	394.6	6.11	4.98	35.65	410.1
5.79	7.48	43.30	451.2	6.01	7.48	40.41	469.0
2.61	0.00	29.02	620.0	2.74	0.00	27.85	657.2
2.51	4.98	33.30	736.2	2.86	4.98	33.09	743.0

In addition to the comparative study presented here, another series of experiments was carried out with the aim of achieving the highest average particle outlet temperature possible in this laboratory setting. Therefore, a smaller particle population with a mean of around 164 µm was used. It was possible to achieve an average particle outlet temperature of around $795\,°\mathrm{C}$ with a thermal efficiency of around 31 % (the corresponding temperature profile is given in figure 17). This record was achieved for a particle mass flow rate of around $2.41\,\mathrm{g\,s^{-1}}$ and an air flow rate of $4.99\,\mathrm{ln\,min^{-1}}$. In a comparable case without the presence of a counter-current air flow, an average particle outlet temperature of around $748\,°\mathrm{C}$ with a thermal efficiency of around 29 % was obtained.

The local wall-to-particles heat transfer coefficient (HTC) is evaluated by a direct measurement of the heat flux on the wall surface $\dot{q}_{wall}$, the particle-laden flow bulk temperature T_{g-p}, as well as the internal wall temperature of the SiC tube $T_{d,int}$

$$h(z) = \frac{\dot{q}_{interface}}{T_{d,int} - T_{d,g-p}} = \frac{k_d(T_{d,ext} - T_{d,int})}{\Delta x_t(T_{d,int} - T_{g-p})} \tag{4}$$

with k_t being the temperature dependent thermal conductivity of the tube material, and Δx_t being the wall thickness of the tube. Figure 19 shows how the local wall-to-particles HTC changes with respect to the particle mass flow rate and air flow rate. When increasing the particle mass flow rate, an increase in the local HTC can be observed. An even more significant increase in local HTC was observed when the counter-current air flow was introduced. Both the increase in particle mass flow rate and the introduction of air flow lead to an increase in the solids volume fraction and have a positive influence on the HTC, which has also been reported for other particle-in-tube receivers..[16] As the air flow leads to a greater change in the solid volume fraction, the local HTC changes more strongly with the air flow.

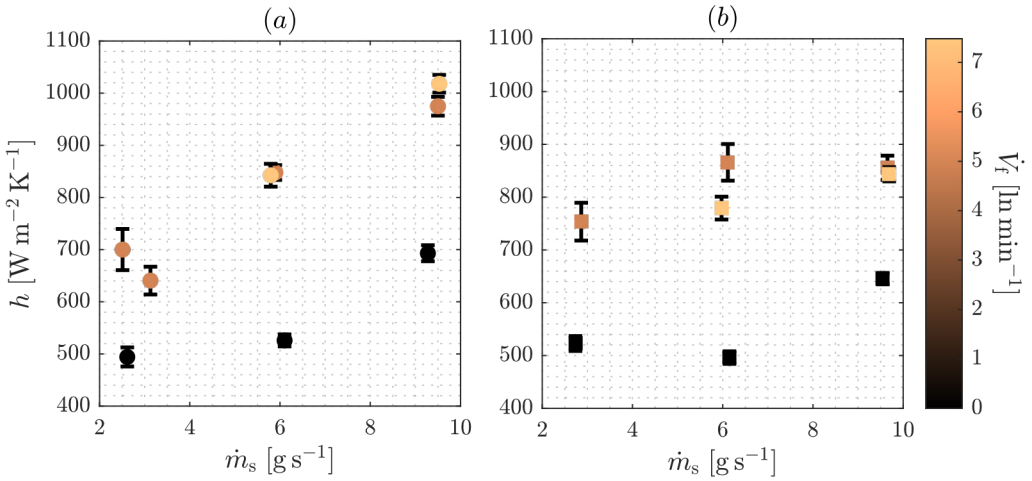

Figure 19: Local wall-to-particle HTC measurements for two different power inputs, (a) $\dot{Q}_{\mathrm{solar}}$ = 5.36 kW and (b) $\dot{Q}_{\mathrm{solar}}$ = 6.21 kW, are given. The HTC is plotted against the particle mass flow rate and the colour of the marker indicates the air flow rate. The vertical bars represent the standard deviation of the observable.

5 Evaluation of Results to Date

The experimental investigation of the CFDR showed that the counter-current air flow decreases the average fall speed of the particles and has a positive influence on the thermal efficiency as well as the outlet temperatures of the particles in direct comparison to scenarios without the presence of air. In the scope of the project, two KPIs in particular were to be investigated, whereby it was possible to demonstrate wall-to-particles HTC greater than 1000 $\mathrm{W\,m^{-2}K^{-1}}$, but not to achieve particle outlet temperatures above $1000\ °C$. It is important to emphasize that the inner wall temperature of the SiC tube, $T_{d,int}$(@z = 0.98 m), reached temperatures well above $795\ °C$ (see figure 17), indicating that the particles could absorb more radiative energy from the tube if the irradiated region of the tube is longer. Because as the length of the irradiated region increases, the particles have more time to exchange heat with the SiC tube.

Research on indirectly irradiated, gravity-driven particle solar receivers has only recently begun, with relatively few published studies available for comparing the CFDR to other receivers within this category.[12,13,29] However, there is general consensus that such a receiver must achieve wall-to-particle heat transfer coefficients of around 1000 $\mathrm{W\,m^{-2}K^{-1}}$, be capable of reaching HTM outlet temperatures exceeding $700\ °C$, while reaching high thermal efficiencies. Smaller wall-to-particle HTCs reflect that the thermal resistance of the indirectly irradiated systems are too high, thereby rendering such a system unattractive for continued development. This first generation lab-scale prototype of the CFDR achieved competitive HTCs and showed that high particle outlet temperatures are feasible. For the future, the goal must be to increase the thermal efficiency further. Yet, to the best of our knowledge, this experimental work is the first one to present thermal efficiency measurements for a counter-current gravity-driven receiver. It is important to keep in mind that the current version of the CFDR is a lab-scale prototype that was already tested under very realistic conditions (no use of pre-heated air or particles; unfavourable surface-to-volume ratio resulting in high thermal losses; use of a HFSS not a furnace). This may be best seen when comparing this work to a study presented by Gueguen et al..[16] They are working on an indirectly irradiated co-current fluidized bed receiver and reported wall-to-particles HTCs as well as thermal efficiencies. For particle mass fluxes similar to the one realized in our study (5 $\mathrm{kg\,m^{-2}s^{-1}}$ to 35 $\mathrm{kg\,m^{-2}s^{-1}}$), they report very comparable HTCs and thermal efficiencies. However, it is important to point out, that this is no longer a lab-scale study making our results promising. One important distinction between the CFDR and the previously discussed designs is the choice of material used within the irradiated zone. While other receivers rely on metallic materials, which limit operating temperatures to around $1000\ °C$, the CFDR employs a ceramic-based design. This not only enables testing at significantly higher temperatures but also represents a unique feature of the CFDR, positioning it as a promising candidate for future applications in very high-temperature regimes.

The future of CSP lies in high-temperature applications, which require particle outlet temperatures exceeding $700\ °C$. This makes molten salt receivers unattractive unless a viable alternative salt is found that enables operation at these temperatures while addressing concerns such as toxicity and material compatibility. Indirectly irradiated receivers face challenges in outperforming directly irradiated ones due to the additional thermal resistance introduced in the heat transfer path (see summary table 4). However, they have other advantages an open-aperture directly irradiated solar particle receiver like the particle curtain receiver will not be able to deliver. An indirectly irradiated receiver enables to work under reaction environments that are different from ambient air, and tackle the issue of particle loss. Further, thermochemical processes often require control of the particle residence time inside the reaction zone, which can not be changed for a particle curtain receiver once constructed. Counter-current, as well as co-current particles-in-tube receiver like the CFDR allow for a certain amount of particle residence time control. If CSP is to expand into a broader range of applications, a variety of solar receiver and reactor designs must be available to ensure that the most suitable solution can be selected based on the specific requirements of each process.

Table 4 Overview of experimentally determined particle outlet temperatures and associated thermal efficiencies across different solar particle receiver designs.

Receiver	*Irradiation*	$\dot{q}_{in}$ [$kW\,m^{-2}$]	T_{out} [°C]	η_{th} [%]	Reference
Particle curtain receiver	direct	680	735	71	[30]
Rotary kiln receiver	direct	670	900	75	[31]
Fluidized bed receiver	indirect	274	600-670	15-25	[16]
CFDR (this study)	indirect	4942	795	31	-

6 Next Steps

In the near future, the analysis of the irradiation campaign data will be finalized and compared to other lab scale solar particle receivers. The findings will be summarized in form of a paper. Afterwards, the numerical simulation of the CFDR will be completed, and the experimental data compared with the numerical results. It is planned to publish the outcome of the numerical study in a second paper. Finally, it will be possible to assess the potential of the counter-current solar receiver in the context of already existing, more established particle solar receivers.

In a broader context, the CFDR is at an early stage of its development making it difficult to compare with the more established SPRs, each of which has been researched for at least a decade. Further work is required in order to gain a more concrete picture of the competitiveness of the CFDR compared to the other SPR types. From an experimental point of view, two possible next steps were identified: (1) Testing the thermal performance of a scaled-up version of the CFDR, or (2) modifying the receiver in such a way, that it is possible to irradiated the particle-laden flow directly. A scale-up of the CFDR would focus on increasing the length over which the ceramic tube is irradiated from the current 0.2 m to about 1m. Yet, it would be necessary to look outside ETH Zurich to find a research facility that can provide an irradiation source with sufficient power and proper geometry to irradiate the larger solar cavity. Changing the concept of the receiver from an indirectly irradiated receiver to a directly irradiated receiver has the potential to further increase the thermal performance of the CFDR as the additional thermal resistance of the ceramic tube is removed. Furthermore, the ceramic tube hinders the current setup to further heat up the cavity as the working temperature of the tube was reached during the irradiation campaign.

To fully evaluate the potential competitiveness of CFDR with respect to alternative power generation technologies, the levelized cost of electricity (LCoE) should be calculated. This represents the cost for building and operating a power plant over its lifetime, expressed on a per kWh basis. This is based on several key parameters beyond the heat transfer and energy conversion performance, including: the upfront investment expenditures, the geographic location, the insurance fees over the facility lifetime, the cost of capital financing, project lifetime, and incentives.[32] In lack of such bases, we may indirectly roughly estimate the LCoE of the proposed technology from the recent estimate provided in a report on the contribution from PROMES-CNRS (France) in the international project G3P3 (Gen 3 Particle Pilot Plant) lead by Sandia National Lab. In such a study, a scaled version of a particle-in-tube receiver is considered whose performance is comparable to the present one, and an LCoE of 0.0467$/kWh is estimated.[33]

The present CFDR concept has been discussed with several leading experts who have visited our department and laboratories at ETH Zurich in recent times, as well as others met at international symposia and conferences. Those include: Prof. Jonathan Scheffe (University of Florida), Prof. Nick AuYeung (Oregon State University), Prof. Thomas Cooper (York University), Prof. Peter Loutzenhiser (Georgia Institute of Technology) and Dr. Zhiwen Ma (National Renewable Energy Laboratory).

They have found the CFDR concept innovative and attractive, recognizing the specific advantages and the complementarity to existing architectures. This provides confidence in the possibility of future international collaboration to develop further the present technology. Directions that have been mentioned as potentially fruitful include: investigating denser particle regimes, potentially by exploring different dispensing architectures, and using high-speed cameras (both infrared and in the visible spectrum) to image directly the temperature of the particles during flow using IR-transparent windows.

7 Communication

- Participation in the poster sessions at the 10th Complex Motion in Fluids Summer School (CMiF2022) in Boekelo, Twente, Netherlands.

8 Conference Contributions

- Presentation at the 19th International Conference on Energy Sustainability (ASME ES 2025), Westminster (CO), United States, 2025
  Role: Technical presentation of 20 minutes about the experimental assessment of the CFDR.
- Presentation at the 4th PhD Colloquium of SFERA-III in Cologne, DLR, Germany, 2023
  Role: Technical presentation of 15 minutes about the CFDR.
- Presentation at the 2023 Multiphase Flow Science Workshop (virtual), 2023
  Role: Technical presentation of 20 minutes about the transparent prototype of the CFDR.

9 References

[1] M. Romero, A. Steinfeld, “Concentrating solar thermal power and thermochemical fuels”, *Energy & Environmental Science* **2012**, *5*, 9234.

[2] M. Romero, J. González-Aguilar, “Solar thermal CSP technology”, *Wiley Interdisciplinary Reviews: Energy and Environment* **2014**, *3*, 42–59.

[3] G. ‘Gus’ Nathan, L. Lee, P. Ingenhoven, Z. Tian, Z. Sun, A. Chinnici, M. Jafarian, P. Ashman, D. Potter, W. Saw, “Pathways to the use of concentrated solar heat for high temperature industrial processes”, *Solar Compass* **2023**, *5*, 100036.

[4] A. H. Alami, A. G. Olabi, A. Mdallal, A. Rezk, A. Radwan, S. M. A. Rahman, S. K. Shah, M. A. Abdelkareem, “Concentrating solar power (CSP) technologies: Status and analysis”, *International Journal of Thermofluids* **2023**, *18*, 100340.

[5] C. K. Ho, “A review of high-temperature particle receivers for concentrating solar power”, *Applied Thermal Engineering* **2016**, *109*, 958–969.

[6] M. Sedighi, R. V. Padilla, R. A. Taylor, M. Lake, I. Izadgoshasb, A. Rose, “High-temperature, point-focus, pressurised gas-phase solar receivers: A comprehensive review”, *Energy Conversion and Management* **2019**, *185*, 678–717.

[7] K. Jiang, X. Du, Y. Kong, C. Xu, X. Ju, “A comprehensive review on solid particle receivers of concentrated solar power”, *Renewable and Sustainable Energy Reviews* **2019**, *116*, 109463.

[8] Y.-L. He, Y. Qiu, K. Wang, F. Yuan, W.-Q. Wang, M.-J. Li, J.-Q. Guo, “Perspective of concentrating solar power”, *Energy* **2020**, *198*, 117373.

[9] M. Mehos, C. Turchi, J. Vidal, M. Wagner, Z. Ma, C. Ho, W. Kolb, C. Andraka, A. Kruizenga, Concentrating Solar Power Gen3 Demonstration Roadmap, National Renewable Energy Laboratory (NREL), **2017**, pp. 1–140.

[10] O. Levenspiel, *Chemical Reaction Engineering, 3rd Edition*, Wiley, **1998**.

[11] K. O. Fong, F. Coletti, “Experimental analysis of particle clustering in moderately dense gas–solid flow”, *Journal of Fluid Mechanics* **2022**, *933*, A6.

[12] K. Jiang, Y. Kong, C. Xu, Z. Ge, X. Du, “Experimental performance of gas-solid countercurrent fluidized bed particle solar receiver with high-density suspension”, *Applied Thermal Engineering* **2022**, *213*, 118661.

[13] J. Martinek, Z. Ma, “A Planar-Cavity Receiver Configuration for High-Temperature Solar Thermal Processes”, *SolarPACES Conference Proceedings* **2024**, *2*, DOI 10.52825/solarpaces.v2i.966.

[14] K. J. Brewster, J. R. Fosheim, W. J. Arthur-Arhin, K. E. Schubert, M. Chen-Glasser, J. E. Billman, G. S. Jackson, “Particle-wall heat transfer in narrow-channel bubbling fluidized beds for thermal energy storage”, *International Journal of Heat and Mass Transfer* **2024**, *224*, 125276.

[15] H. Benoit, I. P. López, D. Gauthier, J.-L. Sans, G. Flamant, “On-sun demonstration of a 750 C heat transfer fluid for concentrating solar systems: Dense particle suspension in tube”, *Solar energy* **2015**, *118*, 622–633.

[16] R. Gueguen, G. Sahuquet, M. Tessoneaud, J.-L. Sans, E. Guillot, A. Le Gal, R. Garcia, S. Mer, A. Toutant, F. Bataille, et al., “Heat transfer in a fluidized bed tubular solar receiver. On-sun experimental investigation”, *Solar Energy* **2023**, *265*, 112118.

[17] L. Lee, P. Ingenhoven, Z. Tian, Z. Sun, A. Chinnici, M. Jafarian, P. Ashman, D. Potter, W. Saw, et al., “Pathways to the use of concentrated solar heat for high temperature industrial processes”, *Solar Compass* **2023**, *5*, 100036.

[18] B. D. Iverson, T. M. Conboy, J. J. Pasch, A. M. Kruizenga, “Supercritical CO2 Brayton cycles for solar-thermal energy”, *Applied Energy* **2013**, *111*, 957–970.

[19] R. Schäppi, D. Rutz, F. Dähler, A. Muroyama, P. Haueter, J. Lilliestam, A. Patt, P. Furler, A. Steinfeld, “Drop-in fuels from sunlight and air”, *Nature* **2022**, *601*, 63–68.

[20] A. Steinfeld, “Solar thermochemical production of hydrogen—a review”, *Solar energy* **2005**, *78*, 603–615.

[21] Q Kang, G. Flamant, R Dewil, J Baeyens, H. Zhang, Y. Deng, “Particles in a circulation loop for solar energy capture and storage”, *Particuology* **2019**, *43*, 149–156.

[22] N. Schroeder, H. E. Bush, K. Albrecht, “Assessment of particle candidates for falling particle receiver applications through irradiance and thermal cycling”, *Journal of Solar Energy Engineering* **2025**, *147*, 031012.

[23] S. Brohez, C. Delvosalle, G. Marlair, “A two-thermocouples probe for radiation corrections of measured temperatures in compartment fires”, *Fire safety journal* **2004**, *39*, 399–411.

[24] A Free and Open Source Monte Carlo Ray Tracing Program for Concentrating Solar Energy Research, *Vol. ASME 2010 4th International Conference on Energy Sustainability, Volume 2*, Energy Sustainability, **2010**, pp. 125–132.

[25] W. Thielicke, R. Sonntag, “Particle Image Velocimetry for MATLAB: Accuracy and enhanced algorithms in PIVlab”, **2021**.

[26] I. P. Lopez, H. Benoit, D. Gauthier, J.-L. Sans, E. Guillot, G Mazza, G. Flamant, “On-sun operation of a 150 kWth pilot solar receiver using dense particle suspension as heat transfer fluid”, *Solar Energy* **2016**, *137*, 463–476.

[27] C. K. Ho, B. D. Iverson, “Review of high-temperature central receiver designs for concentrating solar power”, *Renewable and Sustainable Energy Reviews* **2014**, *29*, 835–846.

[28] V. R. Patil, F. Kiener, A. Grylka, A. Steinfeld, “Experimental testing of a solar air cavity-receiver with reticulated porous ceramic absorbers for thermal processing at above 1000 C”, *Solar Energy* **2021**, *214*, 72–85.

[29] D. C. Miller, C. J. Pfutzner, G. S. Jackson, “Heat transfer in counterflow fluidized bed of oxide particles for thermal energy storage”, *International Journal of Heat and Mass Transfer* **2018**, *126*, 730–745.

[30] C. K. Ho, N. R. Schroeder, H. F. Laubscher, L. Yue, B. Mills, R. Shaeffer, J. M. Christian, K. J. Albrecht in SOLARPACES 2020: 26th International Conference on Concentrating Solar Power and Chemical Energy Systems, Freiburg, Germany, **2022**, p. 110004.

[31] W. Wu, D. Trebing, L. Amsbeck, R. Buck, R. Pitz-Paal, “Prototype testing of a centrifugal particle receiver for high-temperature concentrating solar applications”, *Journal of Solar Energy Engineering* **2015**, *137*, 041011.

[32] M. I. Khan, R Gutiérrez-Alvarez, F. Asfand, Y. Bicer, S. Sgouridis, S. G. Al-Ghamdi, H. Jouhara, M. Asif, T. A. Kurniawan, M. Abid, et al., “The economics of concentrating solar power (CSP): Assessing cost competitiveness and deployment potential”, *Renewable and Sustainable Energy Reviews* **2024**, *200*, 114551.

[33] F. Bataille, G. Flamant, F. Grange, R. Gueguen, A. Le Gal, Assessement of the Fluidized Particle-in-tube technology, Technical, PROMES-CNRS, **2020**.